

## Article

# Preliminary Utility of the Retrospective IMERG Precipitation Product for Large-Scale Drought Monitoring over Mainland China

Linyong Wei <sup>1,2</sup>, Shanhu Jiang <sup>1,2,\*</sup>, Liliang Ren <sup>1,2</sup>, Linqi Zhang <sup>2</sup>, Menghao Wang <sup>2</sup> and Zheng Duan <sup>3</sup>

<sup>1</sup> State Key Laboratory of Hydrology-Water Resources and Hydraulic Engineering, Hohai University, Nanjing 210098, China; 181301010085@hhu.edu.cn (L.W.); RLL@hhu.edu.cn (L.R.)

<sup>2</sup> College of Hydrology and Water Resources, Hohai University, Nanjing 210098, China; zhanglinqi@hhu.edu.cn (L.Z.); mhWang@hhu.edu.cn (M.W.)

<sup>3</sup> Department of Physical Geography and Ecosystem Science, Lund University, S-22362 Lund, Sweden; zheng.duan@nateko.lu.se

\* Correspondence: hik0216@hhu.edu.cn

Received: 15 August 2020; Accepted: 12 September 2020; Published: 15 September 2020



**Abstract:** This study evaluated the suitability of the latest retrospective Integrated Multi-satellite Retrievals for Global Precipitation Measurement V06 (IMERG) Final Run product with a relatively long period (beginning from June 2000) for drought monitoring over mainland China. First, the accuracy of IMERG was evaluated by using observed precipitation data from 807 meteorological stations at multiple temporal (daily, monthly, and yearly) and spatial (pointed and regional) scales. Second, the IMERG-based standardized precipitation index (SPI) was validated and analyzed through statistical indicators. Third, a light–extreme–light drought-event process was adopted as the case study to dissect the latent performance of IMERG-based SPI in capturing the spatiotemporal variation of drought events. Our results demonstrated a sufficient consistency and small error of the IMERG precipitation data against the gauge observations with the regional mean correlation coefficient (CC) at the daily (0.7), monthly (0.93), and annual (0.86) scales for mainland China. The IMERG possessed a strong capacity for estimating intra-annual precipitation changes; especially, it performed well at the monthly scale. There was a strong agreement between the IMERG-based SPI values and gauge-based SPI values for drought monitoring in most regions in China (with CCs above 0.8). In contrast, there was a comparatively poorer capability and notably higher heterogeneity in the Xinjiang and Qinghai-Tibet Plateau regions with more widely varying statistical metrics. The IMERG featured the advantage of satisfactory spatiotemporal accuracy in terms of depicting the onset and extinction of representative drought disasters for specific consecutive months. Furthermore, the IMERG has obvious drought monitoring abilities, which was also complemented when compared with the Remotely Sensed Information using Artificial Neural Networks Climate Data Record (PERSIANN-CDR), Climate Hazards Group Infrared Precipitation with Stations (CHIRPS), and Tropical Rainfall Measuring Mission Multi-satellite Precipitation Analysis (TMPA) 3B42V7. The outcomes of this study demonstrate that the retrospective IMERG can provide a more competent data source and potential opportunity for better drought monitoring utility across mainland China, particularly for eastern China.

**Keywords:** retrospective IMERG; standardized precipitation index; drought monitoring; mainland China

## 1. Introduction

Drought, with its complexity, destructiveness, universality, and extensive influence, is one of the most common natural disasters. It has a serious negative impact on the ecological environment, agricultural productivity, and social development [1–7]. In recent years, continuous global warming, which is mostly caused by human activities (i.e., rapid urbanization- and industrialization-related construction) and the frequent occurrence of natural forest fires (for instance, the 2019–2020 fires in Australia and fires in China over the past two decades) that increase carbon emissions and destroy the environment, has intensified the severity of regional droughts [8–19]. Consequently, in order to conduct a high-precision digital assessment and monitoring regarding the drought evolution process from onset to extinction, it is necessary to establish drought indices according to regional characteristics and to gather high-precision natural variable data, e.g., hydrology and meteorological data [3,6,7,20–23]. These indices and datasets can serve as valuable references for managing water resources, forewarning drought/flood disasters, and decreasing agricultural losses.

Drought indices can be used to identify and appraise drought events, which is conducive to improving our understanding of droughts and their change patterns [3,24–26]. For meteorological drought, there are three frequently used drought indices, i.e., the Palmer drought severity index (PDSI) [20], standardized precipitation index (SPI) [21], and standardized precipitation evapotranspiration index (SPEI) [23]. In 1965, the first practical drought index, PDSI, was developed by Palmer [20]. The PDSI is computed by inputting the initial evapotranspiration and precipitation data, and then utilizing a hydrological model and standardization while considering the water balance theory [7,20,27]. Hence, the traditional PDSI has some defects: It requires multiple climatic variables in the calculation process, and features a single timescale, poor portability, and spatial incomparability [6,8,28]. The SPI developed by McKee et al. was a popular drought index and it only utilizes precipitation data to quantify drought [21]. The SPI features some advantages over the PDSI, e.g., a simpler calculation process, multiple timescales, and greater sensitivity to drought recognition [6,7]. Because of these characteristics, the SPI has become the typically used drought index recommended by the World Meteorological Organization [28–33]. The SPEI, which combines complicated evapotranspiration with ordinary precipitation variables as well, was proposed by Vicente-Serrano et al. [22] based on SPI. The PDSI and SPEI are available to reflect the impact of global warming on drought [20,27,34,35], while they may introduce some impacts of other data sets when only evaluating the usability of satellite precipitation products (SPPs) for drought monitoring. Thus, in this study, we will adopt the SPI.

Precipitation is a momentous meteorological variable and has thus been used as key input to drought indices (e.g., SPI) for drought monitoring [30]. Traditional in situ meteorological stations are the most direct approach to obtain the most accurate precipitation data [6,36]. Because of the sparse and inhomogeneous spatial patterns of meteorological stations and spatiotemporal uncertainty of precipitation, collecting precipitation data can be discontinuous in time and confined in space to remote or terrain-complex regions [37–40]. Gauge-based precipitation datasets that are assembled and interpolated based on meteorological stations exhibit great uncertainty in certain local regions with substantial elevation differences, especially in the data-deficient areas. Therefore, it is difficult to accurately monitor drought characteristics through sparse in situ meteorological stations.

Nowadays, satellite precipitation retrieval algorithms have been continuously improved by using remote sensing data [36], allowing a series of SPPs with high spatial-temporal resolution to be generated and released for free on the internet for public access. Several widely used SPPs include the Precipitation Estimation from the Remotely Sensed Information using Artificial Neural Networks (PERSIANN) Climate Data Record (PERSIANN-CDR) [41], Climate Hazards Group Infrared Precipitation with Stations (CHIRPS) [42], and Tropical Rainfall Measuring Mission (TRMM) Multi-satellite Precipitation Analysis (TMPA) 3B42V7 [43]. The SPPs estimate precipitation globally, and they provide datasets for climate applications for ungauged or data-scarce regions [7,36,44]. Since March 2014, the research and development of the SPPs has entered into the global precipitation measurement (GPM) era from

the TRMM era [45]. The Integrated Multi-satellite Retrievals for GPM (IMERG) precipitation product is produced through using the vast quantities of information from all available TMPA and GPM sensors [46]. The IMERG features global coverage, a high spatiotemporal resolution, and a superior accuracy and reliability in estimating precipitation and snowfall values [45].

SPPs, in combination with reliable drought indices, have become highly feasible programs for drought monitoring in most regions [4,26,28,32,36]. For instance, Sahoo et al. [28] analyzed the SPI calculated based on TMPA products for drought assessment over global land of 50° N/S, and highlighted that the TMPA 3B42V7 performs reasonably well. Guo et al. [30] also utilized the SPI to evaluate PERSIANN-CDR performance for drought monitoring in China, and obtained that it has a good similarity with reference data for drought patterns over the eastern region. Zhong et al. [7] chose the SPI and PDSI to assess and compare the drought monitoring applicability of PERSIANN-CDR, CHIRPS, and TMPA 3B42V7 across China, and summarized that they perform satisfactorily in the eastern region as well, and TMPA 3B42V7 possesses the best performance and great potential for drought monitoring. These results all indicate that the three SPPs products have good reliability for drought monitoring in some regions of China; however, they are not the best precipitation data among the SPPs. The satellite precipitation product with the highest spatiotemporal resolution and optimum dependability among the multi-source SPPs should be used to reduce error propagation in the drought detection process [7]. Recently, some research results have proclaimed that the IMERG Final Run precipitation product is a better dataset compared to other SPPs, i.e., the PERSIANN-CDR, CHIRPS, and TMPA, in Huanghuaihai Plain of China [47] and mainland China [48]. The quality of the IMERG product has been demonstrated to estimate precipitation more reliably. Furthermore, the newest version, IMERG V06, features unique characteristics compared with those of the previous versions, i.e., updated algorithm (including several central improvements for improving the accuracy of IMERG precipitation products) and retrospective processing (creating a longer temporal scale from June 2000 to the present) [48,49]. The central objectives of the retrospective IMERG are to act as a substitute for the widely used TMPA precipitation data, and to be more extensively applied in the field of hydrometeorology, such as for meteorological drought [36,50]. However, the drought monitoring utility of the newly released retrospective IMERG V06 is still unclear.

In consideration of the characteristics of the latest retrospective IMERG, this study aimed to: (i) Evaluate the accuracy of the IMERG Final Run precipitation product by comparing it with in situ precipitation measurements at multiple temporal and spatial scales over mainland China; (ii) investigate the performance of the IMERG Final Run precipitation product for large-scale drought monitoring; and (iii) compare the IMERG Final Run precipitation product against three widely used bias-adjusted SPPs, namely PERSIANN-CDR, CHIRPS, and TMPA 3B42V7. This study provides an example and extension of the application of the newly released retrospective IMERG precipitation data for drought monitoring.

## 2. Study Area, Datasets and Methods

### 2.1. Study Area

China has a vast territory (Figure 1a) with complex topography and diverse landforms. With great differences in the natural climatic and landform characteristics throughout the country, the spatial and temporal distributions of precipitation are extremely complex, i.e., the annual mean precipitation is significantly different in the eastern region (less than 200 mm) compared to that in the western region (over 1600 mm) (Figure 1b). This phenomenon makes China more prone to suffering from drought disasters [6,7]. In this study, to better evaluate the accuracy of the IMERG precipitation dataset and investigate its application for regional drought monitoring, the eight regions previously researched by Chen et al. [51], sub-regions covering mainland China and excluding Taiwan, were selected. Of these regions, region 1 (R1, northeastern China) and region 2 (R2, northern China) are governed by a temperate monsoon climate; region 3 (R3, middle and lower reaches of the Yangtze River), region 4 (R4, southeastern China), and region 5 (R5, southwestern China) are dominated by

a subtropical monsoon climate; region 6 (R6, northwestern China) and region 7 (R7, Xinjiang) give priority to an arid or semi-arid climate, while region 8 (R8, Qinghai-Tibet Plateau) is primarily covered by a plateau mountain climate [51].

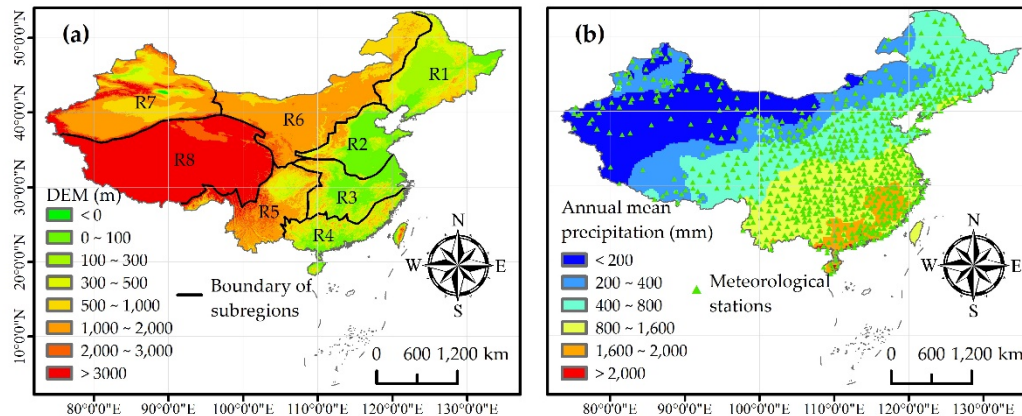


**Figure 1.** (a) Digital elevation model (DEM) and spatial distribution of the eight sub-regions and (b) meteorological stations and annual mean precipitation during 2001–2017 over mainland China. The grid precipitation interpolation was based on the inverse distance weight (IDW) of the precipitation data from 807 meteorological stations. Note: R1: northeastern China, R2: northern China, R3: middle and lower reaches of the Yangtze River, R4: southeastern China, R5: southwestern China, R6: northwestern China, R7: Xinjiang, R8: Qinghai-Tibet Plateau.

## 2.2. IMERG and Other SPPs

The retrospective IMERG, with a comparatively high spatial resolution of  $0.1^\circ$  and multiple temporal resolutions (i.e., 0.5 h, 3 h, 1 day, 3 days, 7 days, and 1 m), was released (<https://pmm.nasa.gov/>) in May 2019 [50]. Compared to the legacy versions, there are some major improvements to the IMERG V06, i.e., adopting the Climate Prediction Center MORPHing technique, in consideration of the Goddard profiling algorithm and Megha-Tropiques Sounder for Probing Vertical Profiles of Humidity, and slightly changing the passive microwave estimation for reducing spatial gaps [48,49]. The IMERG incorporates three different modes of precipitation products, i.e., real-time Early Run, Late Run, and delayed Final Run precipitation data. Of these products, the IMERG Final Run data is calibrated using monthly gauge-based analysis data (i.e., the Global Precipitation Climate Center, hereafter GPCC, V8 Full Data Analysis for the majority of the time, and the GPCC V6 Monitoring Product from 2017 to the then-present) for its accuracy to be close to that of the actual precipitation data [52]. In this study, the retrospective IMERG Final Run precipitation product was primarily used for drought application. The daily IMERG Final Run precipitation data from June 2000 to December 2017 were obtained from the aforementioned website.

PERSIANN-CDR is a new retrospective long-term (from 1983 onward) SPP, with a spatial resolution of  $0.25^\circ$  and spatial coverage of  $60^\circ$  N/S. PERSIANN-CDR is generated from the PERSIANN algorithm using GridSat-B1 infrared data. It is adjusted using the Global Precipitation Climatology Project (GPCP) V2.3 monthly product to maintain the consistency of the two datasets at  $2.5^\circ$  monthly scale throughout the entire record [41]. CHIRPS is designed by the Climate Hazards Group (CHG), and obtained by merging the IR-derived precipitation and the ground station observations (over 20,000 gauges) [42]. The V2.0 product of CHIRPS features a high spatial resolution of  $0.05^\circ$  and spatial coverage of  $50^\circ$  N/S from 1981 to present. The TMPA 3B42V7 product, with short-term precipitation data (from 1998 onward), a spatial resolution of  $0.25^\circ$ , and covering the band of  $50^\circ$  N/S, is supplied by the National Aeronautics and Space Administration (NASA), and also corrected by using monthly GPCC data [43]. In the present study, the monthly PERSIANN-CDR, CHIRPS, and TMPA 3B42V7 products were selected to compare with the precipitation estimation and drought monitoring capabilities of the IMERG Final Run precipitation data.



### 2.3. In Situ Observation Dataset

The daily China Surface Climate Data set version 3.0 (CSCD) possesses the basic meteorological data from 824 ground meteorological stations from 1951 onward, and it can be downloaded from the China Meteorological Data Network (<http://data.cma.cn>) [53]. The CSCD employs a daily average statistical method to dispose of original data, and it contains diverse precipitation historical records, i.e., 8 p.m. to 8 a.m. (half day), 8 a.m. to 8 p.m. (half day), and 8 p.m. to 8 p.m. (day). Moreover, the rigorous quality control method and the Rclimex software package are utilized to guarantee high CSCD quality [53]. In this study, the observed precipitation dataset was screened and extracted from the CSCD by eliminating certain stations that had >30 days accumulated of missing data in a year and >90 days accumulated of missing data in years. Ultimately, a total of 807 stations (Figure 1b) were utilized to assess the performance of IMERG from June 2000 to December 2017. Because the GPM satellite monitors precipitation data daily from 0 a.m. UTC, it is important to avoid time zone and scale discrepancies between the observed precipitation and IMERG product data. The daily observed precipitation data were accumulated based on the measured data at 8 a.m.–8 p.m. and 8 p.m.–8 a.m. in Beijing Time (UTC + 8).

### 2.4. Standardized Precipitation Index (SPI)

The SPI is a well-known and frequently used dimensionless meteorological drought index proposed by McKee et al. in 1993, and it only utilizes precipitation as the drought characterization factor and features less dependence on data [21]. The major SPI procedures are to accumulate precipitation records at several timescales (typically from 1 to 24 m) and then to utilize the Gamma distribution or Pearson III frequency conversion, and the standardized normal distribution to calculate the normalized drought index value [21]. The SPI values are comparable across regions, and the flexibility of the various timescales can reflect drought conditions in different periods (i.e., monthly, seasonal, and annual drought events), including agro-hydrological droughts [6]. The drought categories, in accordance with the SPI values, are listed in Table 1. These ranges were derived from the “Classification of Meteorological Drought” defined by China National Standardization Management Committee [6,54]. The SPI values, with a general numeric range of −3 to +3, were calculated by selecting the Gamma distribution and employing both the retrospective IMERG and monthly observed precipitation data from June 2000 to December 2017, which are denoted as the IMERG-based SPI and gauge-based SPI, respectively. The 1-, 3-, 6-, and 12-month SPIs are abbreviated as SPI1, SPI3, SPI6, and SPI12, respectively.

**Table 1.** Drought classifications in accordance with Standardized Precipitation Index (SPI) values.

Drought Rank	Index Values
No drought	$SPI > -0.5$
Light drought	$-1.0 < SPI \leq -0.5$
Moderate drought	$-1.5 < SPI \leq -1.0$
Severe drought	$-2.0 < SPI \leq -1.5$
Extreme drought	$SPI \leq -2.0$

### 2.5. Statistical Metrics

For the multi-angle IMERG performance evaluation for both the precipitation estimation and drought monitoring utilities, the nearest point-to-pixel (coordinates of meteorological stations) matching approach was instructively employed. Three conventional metrics and one comprehensive statistical metric were used to quantitatively explore the error characteristics of the IMERG precipitation data, i.e., the correlation coefficient (CC) with an optimal value of 1, root mean square error (RMSE) with an optimal value of 0, relative bias (RB) with an optimal value of 0, and Kling–Gupta efficiency (KGE') with an optimal value of 1 [28,38]. The CC describes the level of linear correlation (consistency) of the target (i.e., IMERG or IMERG-based SPI) against the reference data (i.e., observed precipitation or

gauge-based SPI). The RMSE expresses the dispersion degree of the target against the reference data. The RB indicates whether the estimated IMERG product value is greater or smaller with respect to that of the observed precipitation. The KGE' synthetically assesses the contributing capacity of the CC, bias, and variability [48]. The four metrics are defined as:

$$CC = \frac{\sum_{i=1}^n (G_i - \bar{G})(S_i - \bar{S})}{\sqrt{\sum_{i=1}^n (G_i - \bar{G})^2} \sqrt{\sum_{i=1}^n (S_i - \bar{S})^2}}, \quad (1)$$

$$RMSE = \sqrt{\frac{1}{n} \sum_{i=1}^n (S_i - G_i)^2}, \quad (2)$$

$$RB = \frac{\sum_{i=1}^n (S_i - G_i)}{\sum_{i=1}^n G_i} \times 100\%, \quad (3)$$

$$KGE' = 1 - \sqrt{(CC - 1)^2 + (\bar{S}/\bar{G} - 1)^2 + ((\sigma_s/\bar{S})/(\sigma_g/\bar{G}) - 1)^2}, \quad (4)$$

where  $n$  is the length of the timeseries (i.e., 6423 days, 177 months, and 17 years),  $S_i$  is the value of the target at time  $i$ ,  $G_i$  is the value of the reference data at time  $i$ ,  $\bar{G}$  and  $\bar{S}$  are the mean values, and  $\sigma_s$  and  $\sigma_g$  are the standard deviation. The KGEs are in the range of  $[-\infty, 1]$ , where a high value demonstrates superior performance.

To probe the detection capability of the IMERG for drought events or conditions ( $SPI \leq -0.5$ , at least light drought), two frequently used statistical metrics were adopted, i.e., the probability of detection (POD) with an optimal value of 1, and the false alarm rate (FAR) with an optimal value of 0 [7]. The POD represents the fraction of drought conditions correctly monitored by the IMERG of all the drought events quantified by meteorological stations. The FAR reflects the fraction of drought condition incorrectly predicted of all the drought events monitored by the IMERG. These two indicators are defined as:

$$POD = \frac{H}{H + M}, \quad (5)$$

$$FAR = \frac{F}{H + F}, \quad (6)$$

where  $H$  is the number of months where the gauge-based SPI and IMERG-based SPI monitor drought simultaneously,  $M$  is the number of months where the gauge-based SPI does monitor drought but IMERG-based SPI does not, and  $F$  is the number of months where the gauge-based SPI does not monitor drought but IMERG-based SPI does. The PODs and FARs are all in the range of  $[0, 1]$ .

### 3. Results

#### 3.1. Evaluation of IMERG Precipitation at Multiple Temporal and Spatial Scales

Although the IMERG Final Run precipitation data was calibrated by the GPCC gauge-based precipitation data before becoming available to the public, the GPCC features large errors in some regions of China and a comparatively coarse spatial resolution of  $0.25^\circ$  [52,55]. Moreover, the dataset from any new satellite product must be evaluated and validated before application [36]. It is necessary to directly evaluate the accuracy of the IMERG precipitation over mainland China. Figure 2 displays the scatter plots of the daily precipitation values obtained from the IMERG product against the in situ meteorological station at the point scale in the eight subregions and mainland China and the values of

four metrics in the corresponding regions. The timeseries values of all meteorological stations in a region were superposed into a form of a single timeseries. The IMERG performance in various regions features slightly apparent differences. Specifically, the consistency of IMERG against the observed precipitation data is high in most regions in China. The CCs of R1–R6 and mainland China are greater than 0.7, while the CC is 0.52 in R7 where there is less annual precipitation, and 0.64 in R8 where there is a higher altitude. The RMSEs are large in eastern China with heavy precipitation (i.e., RMSE of 10.2 mm/day in R4), and much smaller in regions with less precipitation, especially the RMSE of 1.81 mm/day in R7. Regarding the RB, a sufficient point gathering for the IMERG product against the observed precipitation data is near the oblique (45°) line (Figure 2), although the IMERG moderately overestimates the precipitation (RB below 11.7%) and negligibly underestimates in R7 (RB of −0.6%). The KGE' value is 0.72 in R3, R4, and mainland China; it is in the range of 0.6–0.7 in R1, R2, R5, R6, and R8; and 0.47 in R7, respectively. We found that the daily IMERG precipitation data typically features an outstanding performance in the estimation precipitation and a high CC and KGE' in R1–R6, while there is slight non-determinacy in R7 and R8 where there are sparsely and irregularly distributed meteorological stations.

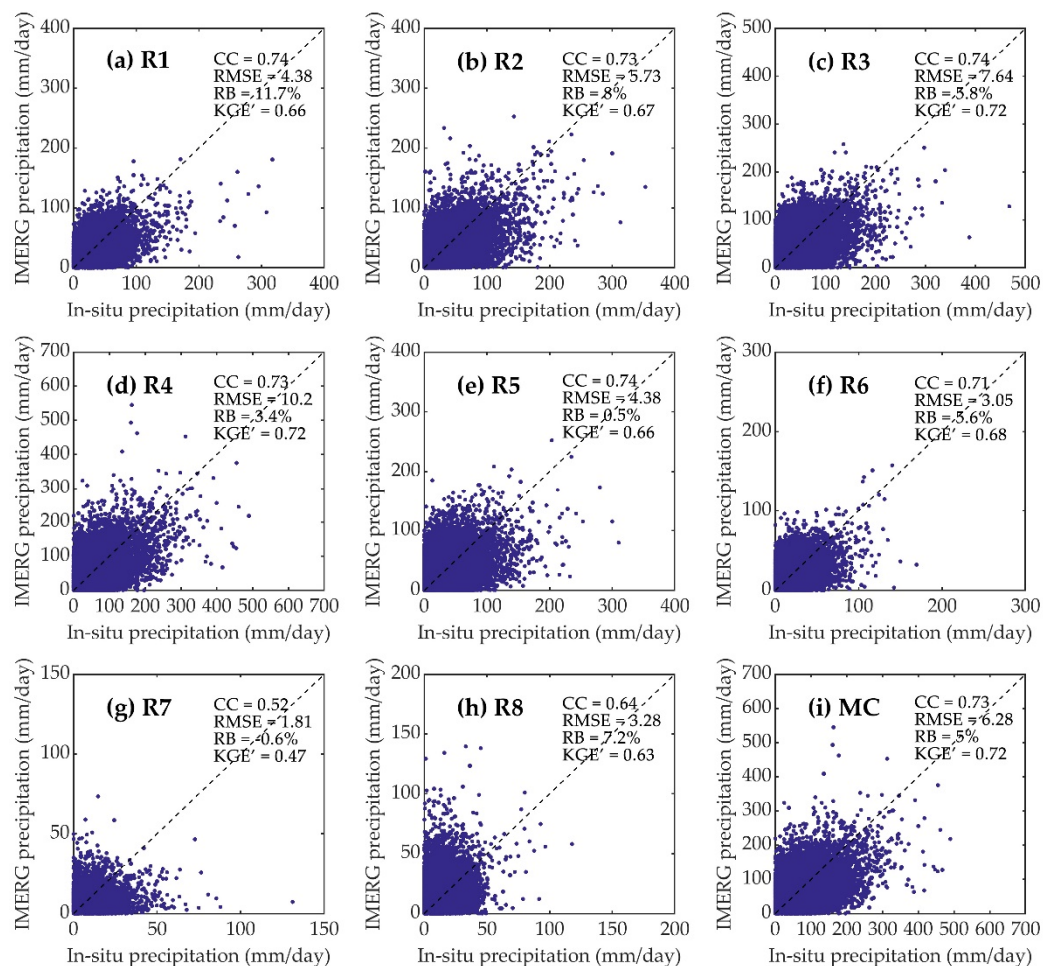


**Figure 2.** Scatterplot and IMERG error statistics, i.e., CC, RMSE (mm/day), RB, and KGE', with respect to in situ precipitation data from meteorological stations at the daily scale for R1–R8 and mainland China (MC). The y-axis represents the IMERG precipitation, and the x-axis represents the in situ precipitation. Note: IMERG: Integrated Multi-satellitE Retrievals for Global Precipitation Measurement, CC: correlation coefficient, RMSE: root mean square error, RB: relative bias, KGE': Kling–Gupta efficiency.

Monthly precipitation is the cumulative total daily precipitation in a month, and annual precipitation is the cumulative total monthly precipitation in a year, except for the year 2000, which exhibited a data deficiency of fewer than 12 months of data. In this study, the daily, monthly, and yearly RBs are nearly the same in terms of spatial pattern and are not shown. The IMERG sufficiently estimates precipitation in R1–R6, with nearly all regions exhibiting RBs of  $-20\%$ – $20\%$ . There is great RB heterogeneity (easily overestimated or underestimated) in R7 and R8, while the mean RB of mainland China is  $10.1\%$ . Figure 3 displays the spatial distributions of the CCs, RMSEs, and KGE's for the IMERG against the observed precipitation data at the daily, monthly, and annual scales.

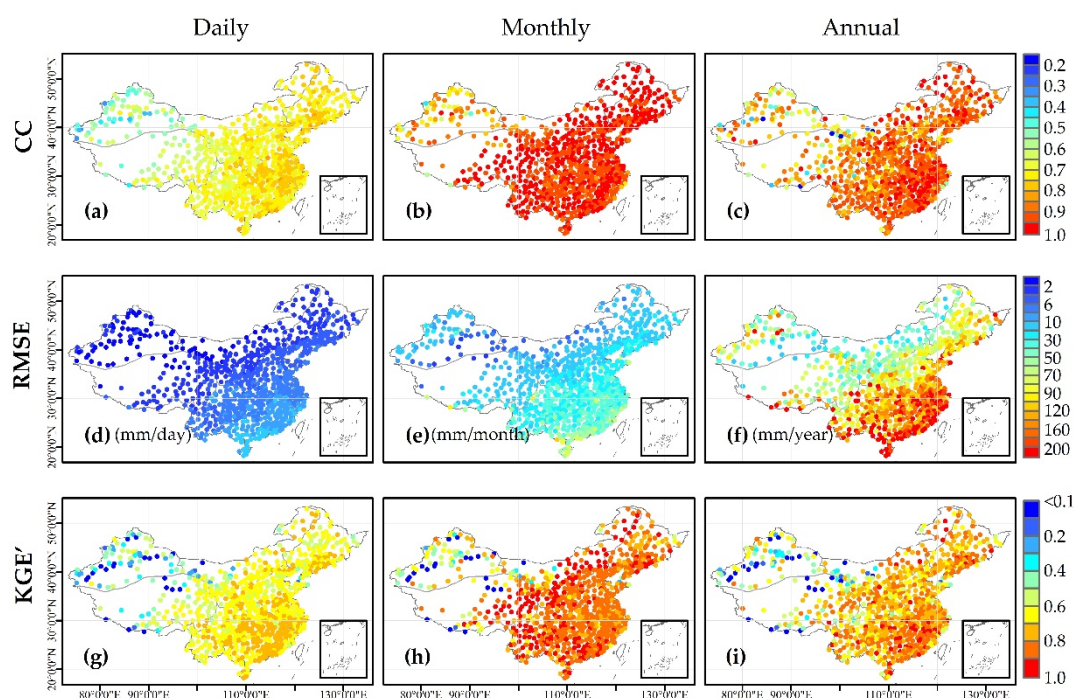


**Figure 3.** Spatial distribution of (a–c) CCs, (d–f) RMSEs, and (g–i) KGE's for the daily, monthly, and annual IMERG data with respect to the precipitation data derived from meteorological stations in mainland China.

The IMERG performance compared to that of the observed precipitation data features obvious discrepancies at different spatial and temporal scales. In particular, there is a greater consistency, comparatively larger error, and improved integration in eastern China, with the humid climate and small differences in regional elevation, compared with that of the western region, with its complex terrain and lower annual mean precipitation. Based on the regional results, the IMERG performs best in R3, with daily, monthly, and yearly mean CCs of 0.74, 0.94, and 0.92; followed by R1, R2, and R4 with identical timescale average CCs of 0.73, above 0.9, and above 0.88; and its worst performance was in R7 with mean CCs of 0.54, 0.78, and 0.73, respectively. As the timescales increase from daily to yearly, the IMERG performance also changes greatly, with daily CCs in the range of 0.3–0.85, monthly CCs in the range of 0.4–1, and yearly CCs in the range of 0.1–1, while in most regions, the daily, monthly, and yearly CC ranges are 0.65–0.8, 0.9–1, and 0.85–0.95, respectively. The KGE's were less than 0.8 at the daily scale and less than 1 at the monthly and yearly scales, while in most regions, the daily, monthly, and yearly ranges were 0.6–0.8, 0.8–1, and 0.6–0.9, respectively. This possibly occurred because the cumulative effect of precipitation offset the partial heterogeneity between the daily IMERG dataset and reference data. The RMSE (Figure 3d–f) is incomparable at different timescales, but it gradually enlarges with an increase in the timescale. There is a strong link between the RMSE spatial distribution and precipitation (Figure 1b), where the RMSE decreases with a decrease in precipitation. The CCs and KGE's increase their optimal values from the northwest to the southeast across mainland China,



and the RMSEs exhibit the opposite trend. Based on the results of other studies, the low IMERG precipitation accuracy in R7 and R8 may be affected by several factors, e.g., the topography, climate, spatiotemporal distribution of precipitation, and generation procedure of the satellite dataset (error correction and retrieval algorithm) [6,7,28,30,47].

Table 2 displays the distributions of the regional CCs, RMSEs, and KGE's at the 0.05, 0.50, and 0.95 quantiles of the daily, monthly, and annual IMERG data against the observed precipitation data for the eight regions and mainland China. The value variation ranges of the monthly CCs and KGE's are smaller than those at the daily and annual scales for the different regions. Additionally, the multiscale CC and KGE' ranges of IMERG in R7 and R8 are broader compared to those in the other regions. Although the CCs and KGE's at the 0.95 quantile are slightly higher (even close to those of R1–R6), they are much lower at the 0.05 quantile (i.e.,  $KGE' < 0$ ). This result may be strongly related to the overlap of the CSCD and GPCC meteorological stations, including an overlap of certain meteorological stations in China [52], and to the sparse-distributed GPCC meteorological stations in western China for IMERG correction and the sophisticated mountainous terrain in this region [47,56]. According to the results of Figure 2, Figure 3, and Table 2, the IMERG possesses a strong capacity for monitoring intra-annual precipitation variations, and it features maximize performance at the monthly scale in comparison with that at the daily and annual scales. Probable causes are that the monthly precipitation eliminates the temporal heterogeneity of daily precipitation to a certain extent, and the annual precipitation diversity of the IMERG against the reference data is obviously larger than that of monthly precipitation, such as Figure 3. Generally, it demonstrates that the retrospective IMERG precipitation is a highly accurate and remarkable potential dataset for quantifying drought.

**Table 2.** The distributions of regional CCs, RMSEs, and KGE's at the 0.05, 0.50, and 0.95 quantiles for daily, monthly, and annual IMERG with respect to precipitation data from meteorological stations in R1–R8 and mainland China (MC).

Regions	Quantiles	Daily			Monthly			Yearly		
		CC	RMSE (mm/day)	KGE'	CC	RMSE (mm/month)	KGE'	CC	RMSE (mm/year)	KGE'
R1	0.05	0.68	3.12	0.54	0.91	11.9	0.71	0.79	49.1	0.61
	0.50	0.74	4.05	0.65	0.96	18.7	0.83	0.91	88.1	0.78
	0.95	0.78	5.82	0.74	0.98	30.1	0.93	0.97	176	0.90
R2	0.05	0.67	3.78	0.57	0.91	14.5	0.73	0.74	52.4	0.58
	0.50	0.73	5.47	0.66	0.95	22.2	0.84	0.90	95.2	0.75
	0.95	0.78	7.60	0.73	0.97	38.9	0.91	0.96	184	0.86
R3	0.05	0.68	5.76	0.61	0.89	22.6	0.77	0.83	86.9	0.68
	0.50	0.75	7.56	0.71	0.94	33.3	0.84	0.93	154	0.80
	0.95	0.79	8.97	0.76	0.97	47.9	0.91	0.97	261	0.91
R4	0.05	0.68	8.11	0.65	0.89	27.5	0.77	0.81	107	0.62
	0.50	0.73	9.56	0.72	0.95	42.3	0.88	0.93	192	0.83
	0.95	0.77	13.8	0.76	0.97	72.2	0.94	0.97	325	0.93
R5	0.05	0.63	4.96	0.55	0.90	20.9	0.72	0.73	67.9	0.57
	0.50	0.70	6.88	0.67	0.95	30.4	0.88	0.89	126	0.76
	0.95	0.75	8.67	0.72	0.98	51.6	0.95	0.95	327	0.88
R6	0.05	0.62	1.27	0.28	0.85	6.57	0.44	0.62	21.0	0.33
	0.50	0.71	2.92	0.66	0.95	11.7	0.88	0.90	49.1	0.75
	0.95	0.77	4.66	0.73	0.98	20.1	0.96	0.97	106	0.93
R7	0.05	0.36	0.65	−0.52	0.62	3.90	−0.41	0.39	14.8	−0.46
	0.50	0.55	1.57	0.36	0.79	10.5	0.58	0.77	50.4	0.48
	0.95	0.69	2.77	0.60	0.93	23.4	0.81	0.92	171	0.79
R8	0.05	0.51	0.94	−0.54	0.79	6.22	−0.43	0.40	33.5	−0.46
	0.50	0.64	3.24	0.58	0.96	14.3	0.87	0.82	71.0	0.69
	0.95	0.72	4.46	0.70	0.98	33.5	0.95	0.94	219	0.86
MC	0.05	0.53	1.41	0.28	0.79	7.84	0.47	0.63	32.7	0.31
	0.50	0.72	5.35	0.67	0.95	22.9	0.85	0.90	102	0.77
	0.95	0.77	10.3	0.75	0.97	54.3	0.94	0.97	277	0.91

### 3.2. Quantitative Evaluation of IMERG-Based SPI

We utilized the IMERG and observed precipitation datasets to calculate the SPI values at 1-, 3-, 6-, and 12-month timescales from June 2000 to December 2017. The CC, RMSE, POD, and FAR were computed based on the IMERG-based SPI values compared to the gauge-based SPI values at the four timescales, which are shown in Figure 4, to assess the reliability and stability of the IMERG-based SPI. The results displayed in Figure 4 reveal that the spatial distributions of the statistical metrics of the IMERG-based SPI are similar to the CCs and KGE's of the monthly IMERG precipitation data, i.e., the optimal performance in R1–R6 with high CCs above 0.8 and low RMSEs below 0.7, and a comparatively poor capability in R7 and R8 at the same timescale. This should be because precipitation is the only input data for the SPI calculation, and the IMERG error is propagated to the SPI. Regarding the IMERG drought detection ability, the spatial distributions of the POD and FAR are similar to that of the CC. There is a strong agreement between the IMERG-based SPI and gauge-based SPI values for drought monitoring in most parts of R1–R6, with PODs over 0.8 and FARs below 0.3. Nevertheless, there are substantial discrepancies and high spatial heterogeneities in most parts of R7 and R8, i.e., the PODs range from 0.5 to above 0.9 and the FARs range from 0.2 to above 0.5. The indicators possess similarities or slight discrepancies at various timescales, i.e., the dependability in the eastern region is superior to that in the western region, and their values slowly increase or decrease in certain regions with an increase in the timescale increment. Therefore, the numeric ranges of the four metrics are widest at the 12-month timescale over mainland China compared with those of the other three timescales. This may be related to the IMERG error in different regions being controlled by systematic or random error.

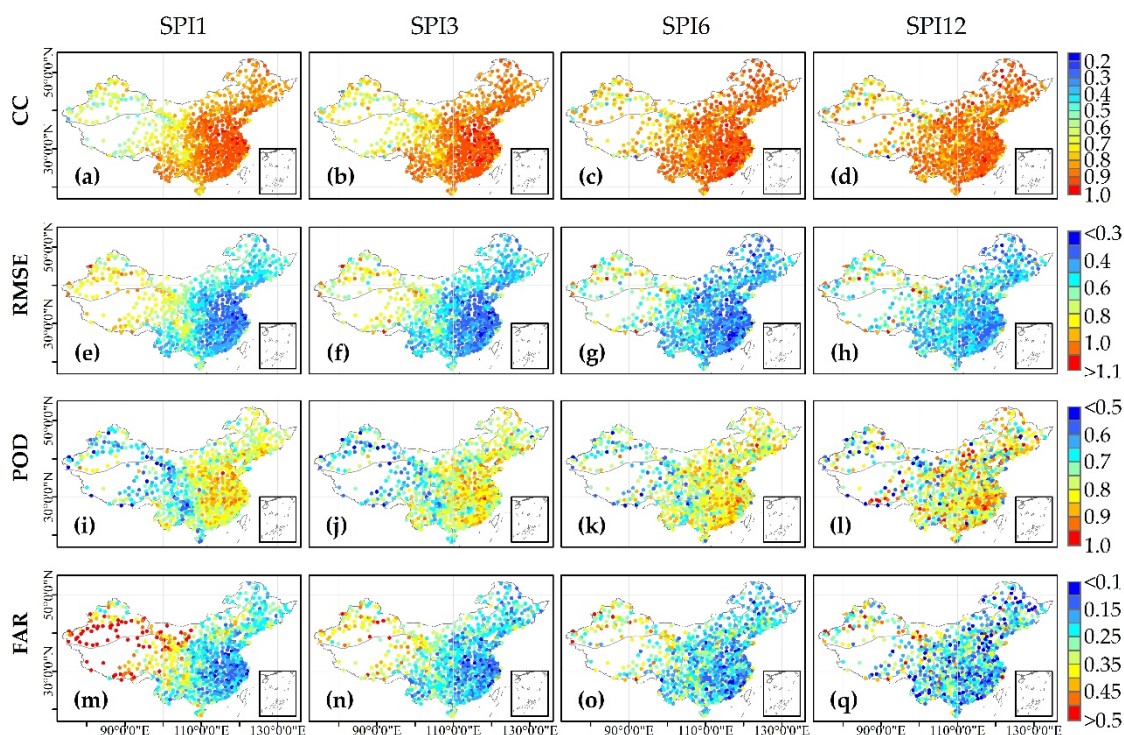


**Figure 4.** Spatial distribution of (a–d) CCs, (e–h) RMSEs, (i–l) PODs, and (m–q) FARs of the IMERG-based SPI values with respect to the gauge-based SPI values at multiple timescales (1-, 3-, 6-, and 12-month) in mainland China.

Figure 5 displays the regional CCs, RMSEs, PODs, and FARs at the 0.25, 0.5, and 0.75 quantiles and their mean values in boxplots; the maximums, 0.99 quantiles, 0.01 quantiles, and minimum values of the metrics were ignored to reduce the influence of outliers. The performance of the IMERG-based SPI is more reliable in R1–R6, while it is less reliable and more uncertain in R7 and R8. The boxplot with

the lower bound at the 0.25 quantile and the upper bound at the 0.75 quantile exhibits the numerical values for the four metrics. (1) In R1–R6, the CCs were beyond 0.74 at the 0.25 quantile; the RMSEs were in the range of 0.3–0.7 between the 0.25 quantile and 0.75 quantile; the PODs were over 0.65 at the 0.25 quantile; and the difference in upper-lower FARs was within 0.2, and the mean value was less than 0.33. (2) In R7 and R8, certain metrics exhibited superior performances (i.e.,  $CC > 0.7$  and  $POD > 0.8$ ), while they exhibited wider value ranges and the mean values were less than those of R1–R6 at the 0.25 quantile. Furthermore, the variations of the indexes at various timescales were not conspicuous in R1–R6, but they were significant in R7 and R8 (i.e., gradually improving the performance from the 1-month to 12-month scales). This was likely related to the sliding accumulation precipitation values at longer timescales eliminating or reducing the temporal heterogeneity of the precipitation to a certain extent. In comparison, the indicators emphasized that the IMERG-based SPI at the 6-month scale performed more optimally, which is displayed in Figure 4. Overall, the retrospective IMERG performed well for drought monitoring in most regions of mainland China by utilizing the SPI.

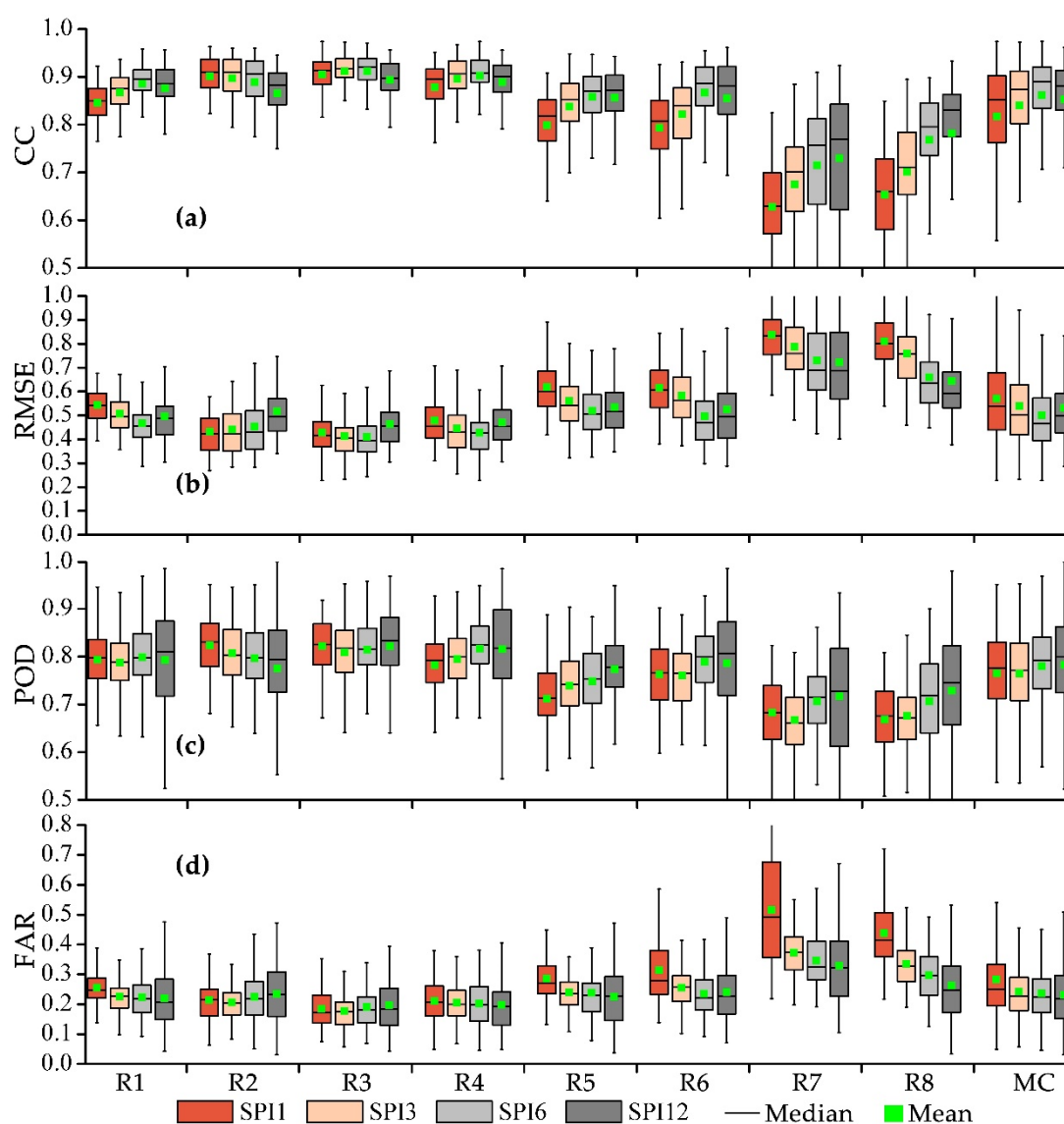


**Figure 5.** Boxplots of the (a) CCs, (b) RMSEs, (c) PODs, and (d) FARs of the IMERG-based SPI with respect to the gauge-based SPI at multiple timescales (1-, 3-, 6-, and 12-month) for R1–R8 and mainland China (MC).

### 3.3. Regional Validation of IMERG-Based SPI for Drought Events

The performance of the IMERG-based SPI was further evaluated and explored spatiotemporally regarding the regional drought characteristics (i.e., drought intensity and area) of R1–R6 using high-accuracy precipitation data. Due to the sparse-distributed meteorological stations and uncertain data, R7 and R8 were not considered in this evaluation. The SPI6 was chosen for the detailed assessment due to its superior results. Figure 6 displays the drought intensity quantified by the regional mean SPI6 and ratio of drought area, which was roughly measured by the percentage (the number of meteorological stations experiencing drought conditions versus the total number meteorological stations in the region), for the six regions in the timeseries. The drought condition threshold value was  $-0.5$  (light drought) for SPI6. The temporal CCs and RMSEs of the regional mean IMERG-based SPI6 compared to those of the gauge-based SPI6 are given in Table 3. The regional IMERG-based SPI6 can precisely portray the onset and extinction of representative drought events of R1–R6 (including intensity and area), even when there were some biases found in the drought estimations (Figure 6). Furthermore, the SPI6 of the IMERG agrees well with that of the observation data (temporal CCs over 0.96 and RMSEs below 0.16). The performance of the regional mean SPI typically outperforms that of the pointed SPI. This is likely because the spatial discrepancies of the IMERG are offset by spatial averaging. In R1 and R6, the IMERG exhibits a comparatively poor consistency compared to that of the reference data, but it can still distinguish the drought process (high CCs and low RMSEs). These results highlight that the IMERG exhibits a satisfactory temporal accuracy.

**Table 3.** Temporal distributions of CCs and RMSEs of the regional mean IMERG-based SPI6 and regional ratio of drought area quantified by the IMERG-based SPI6 for R1–R6 according to Figure 6 and spatial CCs and RMSEs of the representative drought process in southern China for the R2–R5 according to Figure 7.

Regions	Regional Mean Drought Index (Figure 6)		Regional the Ratio of Drought Area (Figure 6)		Spatial Statistical Indicators of Drought Index in Selected Months (Figure 7)		
	CC	RMSE	CC	RMSE	Date (2011)	CC	RMSE
R1	0.962	0.078	0.985	0.150	March	0.924	0.421
R2	0.974	0.068	0.992	0.116	April	0.913	0.451
R3	0.985	0.052	0.996	0.099	May	0.895	0.489
R4	0.988	0.052	0.996	0.098	June	0.801	0.543
R5	0.964	0.06	0.987	0.123			
R6	0.966	0.059	0.985	0.124			

Spatial maps of the drought events roughly identified by the IMERG-based SPI6 and gauge-based SPI6 in specific consecutive months for southern China are exhibited in Figure 7, where they describe a light–extreme–light drought process from March 2011 to June 2011 [57] and crippling drought in April and May. Southern China is a major agricultural production base and includes multitudinous prosperous urban areas, which encompassed R2–R5 in this study. The subareas of Southern China exhibit similar characteristics of the spatial mean SPI6 (i.e., the smallest negative values of the drought index), which are displayed in Figure 6. Table 3 also illustrates the spatial CCs and RMSEs of the IMERG compared to those of the reference data, which were used to quantify the precision in depicting the change processes of the representative drought disasters from Figure 7. The historical drought records of R6 in 2009–2010 are approximately distinguished by the SPI6 [6,7,27], but they were not selected for this study. The results demonstrate that the SPI6 of the IMERG imitates the spatial shape of the drought events accurately (including the areal extent, spatial kernel, and overall movement direction), and agrees with those of the observed precipitation (spatial CCs above 0.8 and RMSEs below 0.55 in the four months), despite a spatial pattern of drought being marginally underestimated (March 2011 in R2). During the drought evolution process, the spatial compatibility of the IMERG gradually decreases with respect to the reference data, while the spatial high CC of 0.801 and low



RMSE of 0.543 occurred in June 2011. The results displayed in Figures 6 and 7 indicate that the IMERG features a typically satisfactory potential for reflecting the spatiotemporal characteristics of drought.

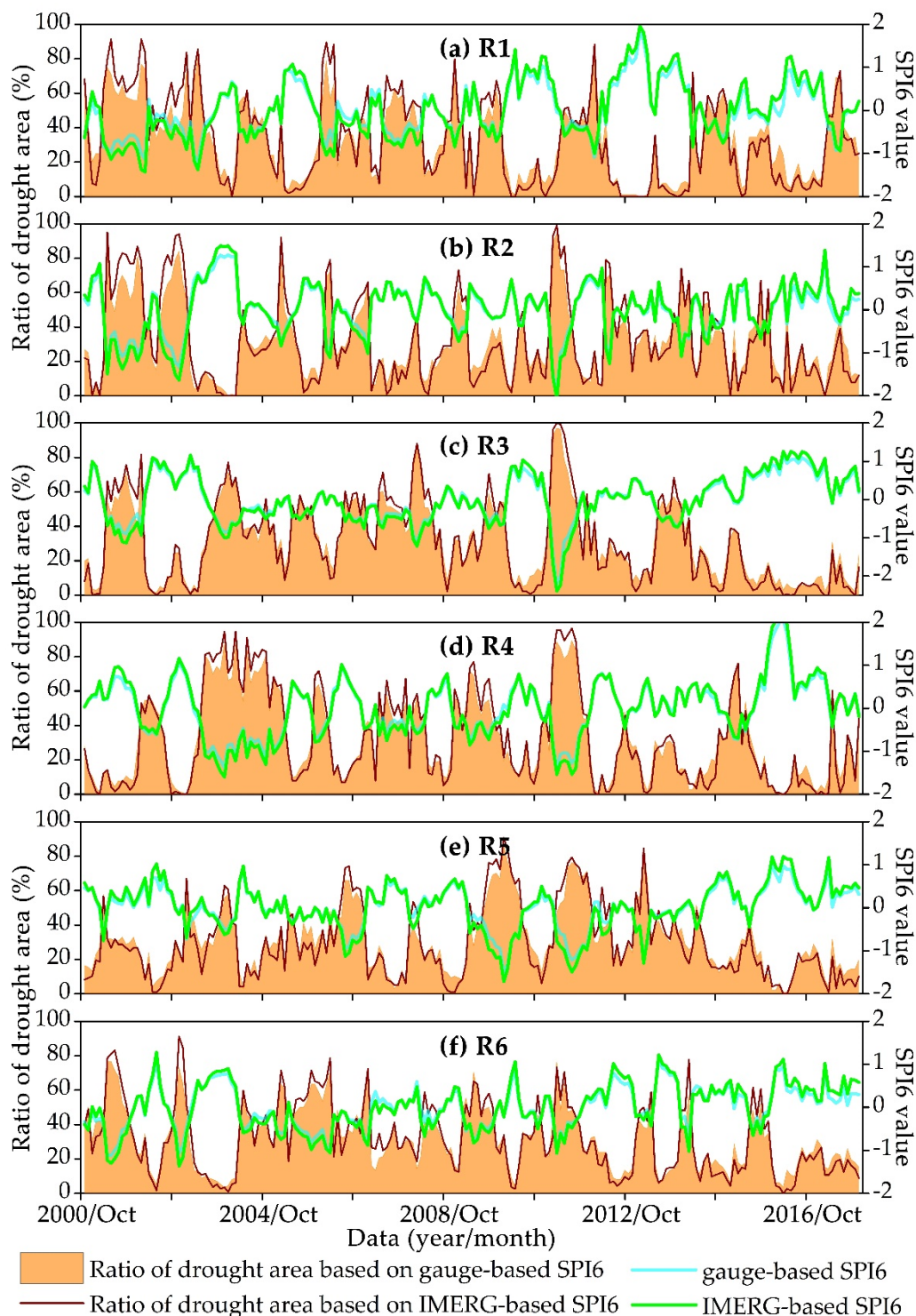


**Figure 6.** Spatial mean SPI6 (right  $y$ -axis) and ratio of drought area (left  $y$ -axis, the ratio of the number of meteorology stations with drought conditions to the total number of meteorology stations in the region) based on SPI6 values in the timeseries.

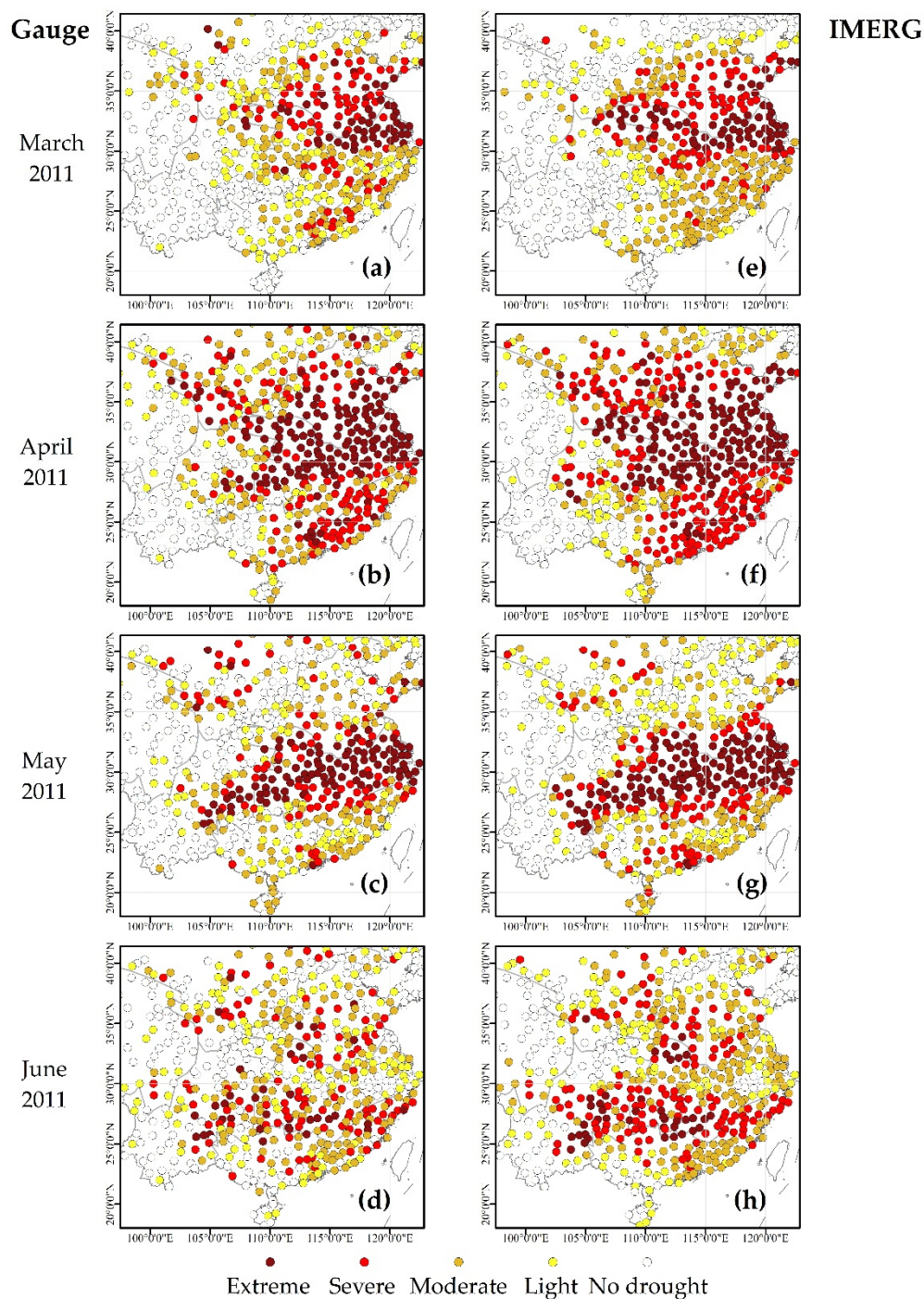


**Figure 7.** Spatial monthly map of SPI6 based on (a–d) gauge precipitation and (e–h) IMERG data for continuous drought events in southern China for R2–R5 from March 2011 to June 2011.

## 4. Discussion

### 4.1. Usability of Retrospective IMERG-Based SPI

In terms of the results above, it illustrated some significant conclusions for the IMERG Final Run precipitation product from multiple perspectives. Namely, the IMERG possesses sufficient stability and reliability in capturing intra-annual precipitation variations and detecting drought over mainland China, although there is a lower accuracy in local regions, such as R7 and R8 [51]. This lower accuracy

is likely due to the topography, climate, precipitation spatiotemporal distribution, and satellite dataset generation procedure (error correction and retrieval algorithm) [6,7,28,30,47].

In view of the retrieval algorithm, it directly affects the SPPs accuracy. Here, we discuss the impact of the retrospective period (retrospective algorithm) on IMERG rainfall accuracy. IMERG V06, the latest version after the retrospective treatment, established a homogeneous record with the TMPA data (beginning in June 2000), allowing the full IMERG precipitation product to cover two periods, i.e., the retrospective period from 1 June 2000 to 11 March 2014 and the GPM period from 12 March 2014 to now [45,49]. Figure 8 shows the regional mean CCs, RBs, and RMSEs (mm/day) of the IMERG precipitation data compared to the observed precipitation data at the daily scale for R1–R8 in the three periods, i.e., the entire period, GPM period, and retrospective period. The precision of IMERG precipitation data in the GPM period is the highest, while that in the retroactive period is slightly low. This embodies that the retrospective precipitation data features a small negative but acceptable impact on the product quality (the differences in CCs are below 0.05, and the differences in RBs are below 4%, except for R7, and the differences in RMSEs are less than 1 mm/day). Compared with the GPM period, there is still room for improvement for the retrospective period of IMERG. Generally, the accuracies of IMERG in the two periods are consistent and comparable over mainland China.

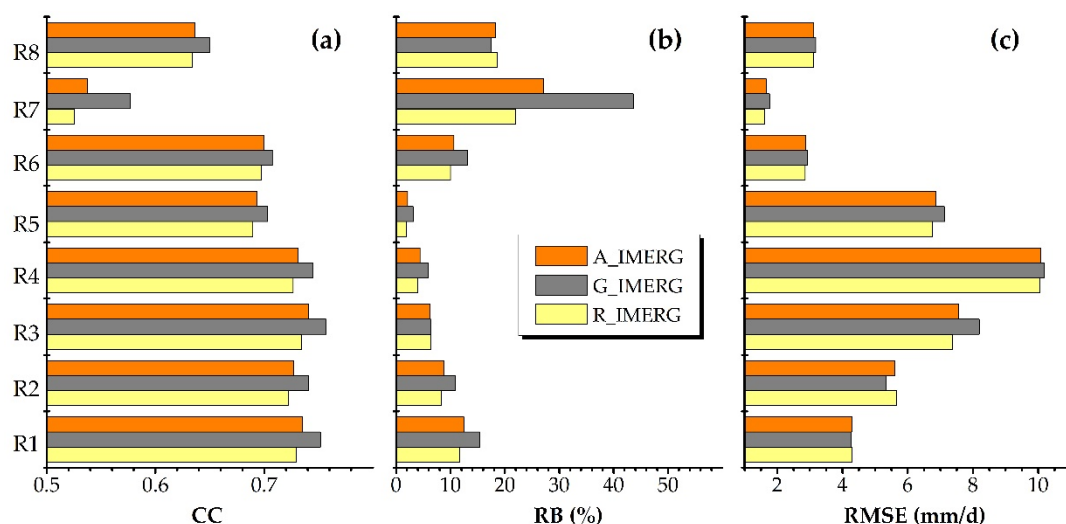


**Figure 8.** Regional mean CCs, RBs, and RMSEs (mm/day) of the IMERG compared to those of the observed precipitation at the daily scale for R1–R8 in the entire, GPM and retrospective periods. Note: A\_IMERG represents the IMERG data for the entire period, G\_IMERG represents the IMERG data for the GPM period, and R\_IMERG represents the IMERG data for the retrospective period.

In this study, we primarily evaluated the suitability of the post-process IMERG Final Run precipitation product for drought monitoring in mainland China. Although near real-time IMERG Early Run and Late Run precipitation products without error correction exist, their accuracies present an apparent low agreement with the IMERG Final Run precipitation product [38,39,52]. Due to the poor reliability of the near real-time IMERG Early Run and Late Run precipitation products in capturing precipitation in most regions, especially in the region with sparse meteorological stations [7,28], it need be considered bias correction before application for monitoring near real-time drought. Consequently, in order to further reveal the importance of the IMERG Final Run precipitation product, the spatial patterns of the KGE's (for precipitation), CCs, PODs, and FARs (for drought) of the IMERG Early Run, Late Run, and Final Run precipitation products against reference data are shown in Figure 9. The IMERG Final Run precipitation product with a regional mean KGE' of 0.79 has an outstanding performance compared with IMERG Early Run and Late Run precipitation products (with a regional mean KGE' of 0.61). When they were applied to drought monitoring, their performance differences were more obvious. The mean CCs of the SPI3 calculated on the IMERG Early Run, Late Run, and



Final Run precipitation products with respect to the gauge-based SPI3 were 0.61, 0.63, and 0.84; their PODs were 0.62, 0.63, and 0.76; and their FARs were 0.4, 0.39, and 0.24, respectively. Hence, there are significant improvements in the performance of the IMERG Final Run precipitation product through bias correction. Additionally, the IMERG Final Run precipitation product, with a short-term (about 20 a) series question that will be effectively settled with the development of GPM [36,48], can be applied in drought monitoring and analysis in terms of previous studies [28,54].

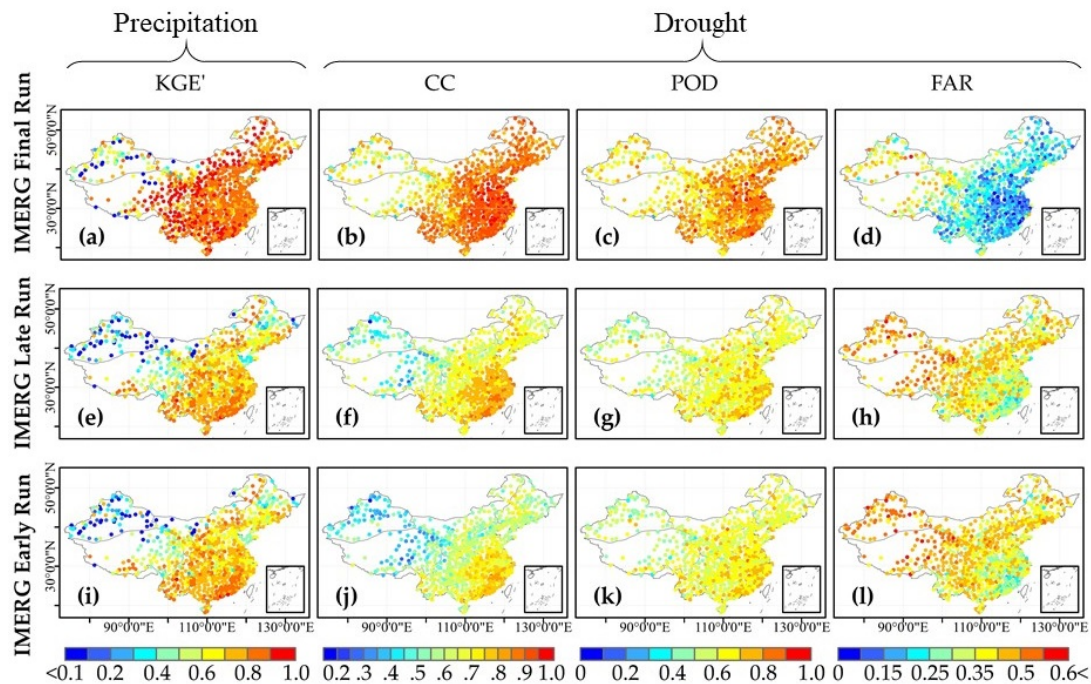


**Figure 9.** Spatial distributions of (a,e,i) KGE's at the monthly scale for precipitation, and (b,f,j) CCs, (c,g,k) PODs, and (d,h,l) FARs of the SPI3 calculated based on the IMERG Early Run, Late Run, and Final Run precipitation products vs. the gauge-based SPI3 for drought in China.

#### 4.2. Does the Retrospective IMERG Feature Significant Advantages Compared to Other SPPs for Drought Monitoring?

In mainland China, Guo et al. [30], Zhong et al. [7], and Bai et al. [27] evaluated and/or contrasted the adaptability of PERSIANN-CDR, CHIRPS, and TMPA 3B42V7 in drought monitoring. Their results unanimously indicated that the three SPPs perform satisfactorily in describing spatiotemporal drought in eastern China, while they are comparatively less accurate in western China, especially in Xinjiang and Qinghai-Tibet Plateau. In this study, similar results were also obtained for the latest retrospective IMERG data. Therefore, we aimed to further conclude whether the retrospective IMERG data with a 0.1° spatial resolution features significant advantages against the three widely used SPPs for drought monitoring. The PERSIANN-CDR, CHIRPS, and TMPA 3B42V7 were chosen to discriminate the significant ability of the retrospective IMERG for drought monitoring.

Figure 10 presents the spatial distributions of the CCs, RBs, and KGE's of the IMERG, PERSIANN-CDR, CHIRPS, and TMPA 3B42V7 against in situ precipitation data. The three statistical indicators of the four SPPs featured a similar spatial pattern characteristic: Namely, they tended to the preferable values in eastern China compared with those in western China. There was high reliability and good consistency between the SPPs and reference data, and the CCs exceeded 0.8 in most regions, even including part of R8. The SPPs all obviously overestimated or underestimated the precipitation in R7 and R8, especially for PERSIANN-CDR, with the absolute RBs over 40% of around 12% stations, while the RBs in R1–R6 varied with the range of −20–20%. Because the CC and RB are inputs to compute the KGE' value, its spatial pattern contained the spatial characteristics of CC and RB, such



as  $KGE'$  corresponding to CC in R1–R6, and it corresponding to RB in R7 and R8. Comparatively speaking, the retrospective IMERG, with a mean CC of 0.93, RB of 10.1 %, and  $KGE'$  of 0.79, possesses the best performance in precipitation estimation over mainland China, then followed by TMPA 3B42V7 with a mean  $KGE'$  of 0.74.

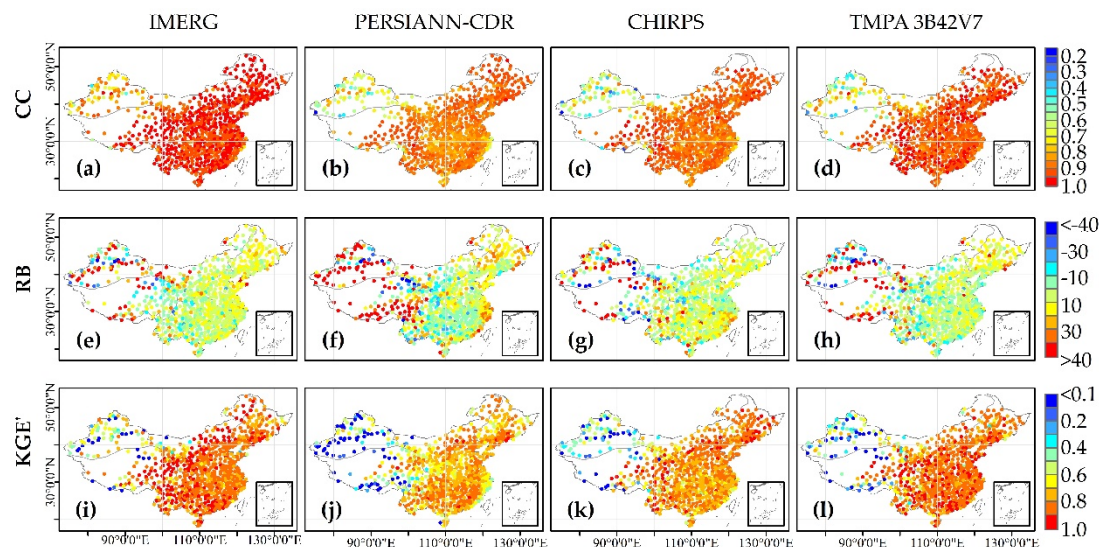


**Figure 10.** Spatial distributions of (a–d) CCs, (e–h) RBs, and (i–l)  $KGE'$ s at the monthly timescale for IMERG, PERSIANN-CDR, CHIRPS, and TMPA 3B42V7 versus in situ precipitation data.

Figure 11 displays the spatial patterns of the CCs, PODs, and FARs of the four SPPs-based SPI6s from November 2000 to December 2017. We can clearly see that the retrospective IMERG exhibits a significant advantage with respect to the other three SPPs in detecting droughts in China. The regional mean CCs of the IMERG-based, PERSIANN-CDR-based, CHIRPS-based, and TMPA 3B42V7-based SPI6 in China were 0.86, 0.69, 0.74, and 0.77, respectively. The IMERG-based SPI6 has a clear superiority and the lowest spatial heterogeneity, with the highest PODs and lowest FARs, in contrast with those of the other three SPP-based SPI6s. This may be because the number of IMERG sensors (covering all available sensors of the TMPA and GPM) is greater than that of the other three SPPs and the IMERG data is adjusted by using the GPCC data with abundant observation stations [46,52]. Nevertheless, the infrared-based PERSIANN-CDR is corrected by coarse-scale GPCP [41,58], and CHIRPS utilizes relatively fewer meteorological stations for bias correction compared with IMERG [42,59]. TMPA 3B42V7 has comparatively fewer sensors than IMERG, although it is also adjusted by GPCC data [43,60]. Generally, among the numerous and continuously upgraded SPPs, the retrospective IMERG precipitation product may be an ideal dataset to surmount the challenges of data limitations to monitor drought [4,36,61].

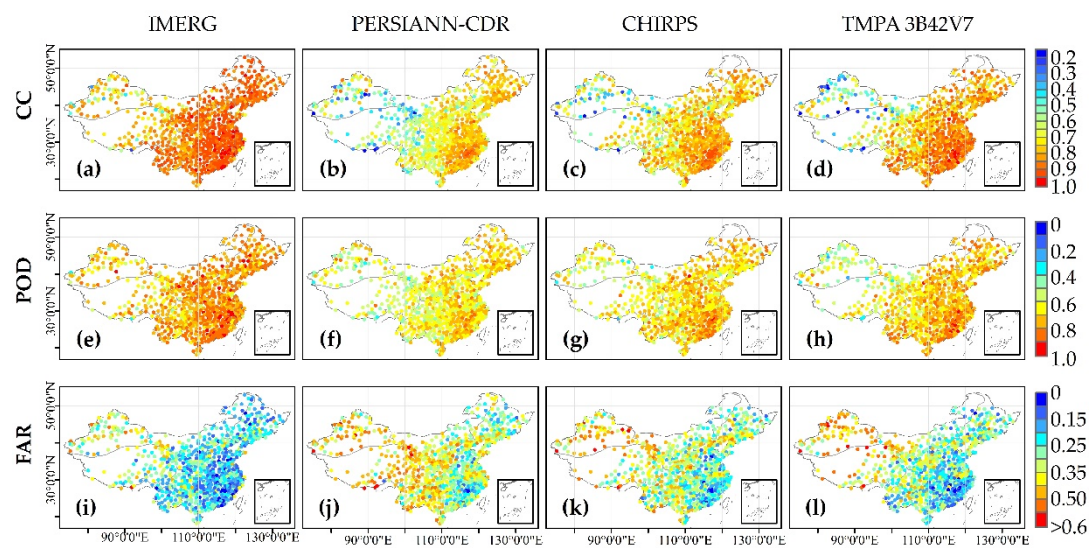


**Figure 11.** Spatial distributions of (a–d) CCs, (e–h) PODs, and (i–l) FARs of the SPP-based SPI6s with respect to the gauge-based SPI6, including the IMERG, PERSIANN-CDR, CHIRPS, and TMPA 3B42V7.

## 5. Conclusions

This study evaluated the error characteristics of the latest retrospective IMERG Final Run precipitation product and verifies its potential utility for drought monitoring from June 2000 to December 2017 in mainland China. Several primary findings were obtained, and they can be summarized as follows:

- (1) Spatially, the IMERG has good agreement with the observed precipitation data in most regions, and there are obvious discrepancies in the Xinjiang and Qinghai-Tibet Plateau regions. Temporally, the IMERG possesses a strong capacity for estimating intra-annual precipitation changes (regional mean CC over 0.7), and it features the best performance at the monthly scale (most CCs above 0.9). The highly accurate and significantly reliable monthly IMERG precipitation is an important data source for drought monitoring.
- (2) The IMERG-based SPI performed well for drought monitoring in most regions over mainland China (with CCs above 0.8), while it exhibited comparatively poor stability in Xinjiang and Qinghai-Tibet Plateau. As the timescale incremented from 1 to 12 months, the accuracy of the IMERG-based SPI correspondingly increased or decreased in certain regions.
- (3) With regard to the regional drought characteristics (i.e., drought intensity and area), the IMERG precisely depicted the onset and extinction of representative drought events (with temporal CCs over 0.96 and RMSEs below 0.16), and it imitated precisely the spatial drought shapes of the specific four-month period (with spatial CCs above 0.8 and RMSEs below 0.55).
- (4) Although the retrospective IMERG features some uncertainties in both precipitation estimation and drought monitoring, it clearly outperforms the other three widely used post-process SPPs, i.e., PERSIANN-CDR, CHIRPS, and TMPA 3B42V7.

In summary, the retrospective IMERG Final Run precipitation product has considerable potential for drought monitoring in most regions of China, while there are relatively high uncertainties in Xinjiang region with light precipitation and the Qinghai-Tibet Plateau region with a high altitude in western China. Overall, our results demonstrated that the retrospective IMERG can be a valuable data source for overcoming data limitations to monitor drought in the future.

**Author Contributions:** Conceptualization, S.J.; Formal analysis, L.W.; Funding acquisition, S.J. and L.R.; Methodology, L.W.; Project administration, L.R.; Resources, L.R.; Software, L.Z.; Supervision, Z.D.; Validation, M.W.; Writing—original draft, L.W.; Writing—review & editing, L.W. All authors have read and agreed to the published version of the manuscript.

**Funding:** This work was financially supported by the National Key Research and Development Program approved by Ministry of Science and Technology, China (2016YFA0601500); the National Natural Science Foundation of China (51979069); the Fundamental Research Funds for the Central Universities (B200204029, 2019B10414); the National Natural Science Foundation of Jiangsu Province, China (BK20180512).

**Acknowledgments:** The IMERG precipitation product used in this study was acquired from the National Aeronautics and Space Administration (<https://gpm.nasa.gov/GPM>). The reference data was provided by the National Meteorological Information Center (NMIC) and China Meteorological Administration (CMA) (<http://data.cma.cn/>).

**Conflicts of Interest:** This manuscript has not been published or presented elsewhere in part or in entirety and is not under consideration by another journal. We have read and understood your journal's policies, and we believe that neither the manuscript nor the study violates any of these. There are no conflicts of interest to declare.

## References

1. Wilhite, D.A. Drought as a natural hazard: Concepts and definitions. In *Drought, a Global Assessment*; Wilhite, D.A., Ed.; Routledge: London, UK, 2000; Volume 1, pp. 3–18.
2. Kao, S.C.; Govindaraju, R.S. A copula-based joint deficit index for droughts. *J. Hydrol.* **2010**, *380*, 121–134. [[CrossRef](#)]
3. Mishra, A.K.; Singh, V.P. A review of drought concepts. *J. Hydrol.* **2010**, *391*, 202–216. [[CrossRef](#)]
4. AghaKouchak, A.; Farahmand, A.; Melton, F.S.; Teixeira, J.; Anderson, M.C.; Wardlow, B.D.; Hain, C.R. Remote sensing of drought: Progress, challenges and opportunities. *Rev. Geophys.* **2015**, *53*, 452–480. [[CrossRef](#)]
5. Lai, C.; Zhong, R.; Wang, Z.; Wu, X.; Chen, X.; Wang, P.; Lian, Y. Monitoring hydrological drought using long-term satellite-based precipitation data. *Sci. Total Environ.* **2019**, *649*, 1198–1208. [[CrossRef](#)]
6. Xu, Z.; Wu, Z.; He, H.; Wu, X.; Zhou, J.; Zhang, Y.; Guo, X. Evaluating the accuracy of MSWEP V2. 1 and its performance for drought monitoring over mainland China. *Atmos. Res.* **2019**, *226*, 17–31. [[CrossRef](#)]
7. Zhong, R.D.; Chen, X.H.; Lai, C.G.; Wang, Z.L.; Lian, Y.Q.; Yu, H.J.; Wu, X.Q. Drought monitoring utility of satellite-based precipitation products across mainland China. *J. Hydrol.* **2019**, *568*, 343–359. [[CrossRef](#)]
8. Dai, A. Characteristics and trends in various forms of the palmer drought severity index during 1900–2008. *J. Geophys. Res. Atmos.* **2011**, *116*, 1248–1256. [[CrossRef](#)]
9. Trenberth, K.E. Changes in precipitation with climate change. *Clim. Res.* **2011**, *47*, 123–138. [[CrossRef](#)]
10. IPCC. *Climate Change 2013: The Physical Science Basis. Contribution of Working Group I to the Fifth Assessment Report of the Intergovernmental Panel on Climate Change*; Cambridge University Press: Cambridge, UK; New York, NY, USA, 2013.
11. Mishra, V.; Lillhare, R. Hydrologic sensitivity of Indian sub-continental river basins to climate change. *Glob. Planet. Chang.* **2016**, *139*, 78–96. [[CrossRef](#)]
12. Venkataraman, K.; Tummuri, S.; Medina, A.; Perry, J. 21st century drought outlook for major climate divisions of Texas based on CMIP5 multimodel ensemble: Implications for water resource management. *J. Hydrol.* **2016**, *534*, 300–316. [[CrossRef](#)]
13. Ali, G.; Pumijumnon, N.; Cui, S. Decarbonization action plans using hybrid modeling for a low-carbon society: The case of Bangkok Metropolitan Area. *J. Clean. Prod.* **2017**, *168*, 940–951. [[CrossRef](#)]
14. Wang, M.; Jiang, S.; Ren, L.; Xu, C.; Yuan, F.; Liu, Y.; Yang, X. An approach for identification and quantification of hydrological drought termination characteristics of natural and human-influenced series. *J. Hydrol.* **2020**, 125384. [[CrossRef](#)]
15. Li, X.; Jin, H.; He, R.; Huang, Y.; Wang, H.; Luo, D.; Yu, S. Effects of forest fires on the permafrost environment in the northern da xing'anling (hingan) mountains, northeast china. *Permafr. Periglac.* **2019**, *30*, 163–177. [[CrossRef](#)]
16. Collins, L.; Bennett, A.F.; Leonard, S.W.J.; Penman, T.D. Wildfire refugia in forests: Severe fire weather and drought mute the influence of topography and fuel age. *Glob. Chang. Biol.* **2019**, *25*, 3829–3843. [[CrossRef](#)]
17. Etchells, H.; O'Donnell, A.J.; Lachlan McCaw, W.; Grierson, P.F. Fire severity impacts on tree mortality and post-fire recruitment in tall eucalypt forests of southwest Australia. *For. Ecol. Manag.* **2020**, *459*, 117850. [[CrossRef](#)]

18. Shuttleworth, K. *Australia Fire Crisis Fuels Protests Calling for Bolder Action on Climate Change: Thousands Protest in Cities as Prime Minister Scott Morrison Defends His Government's Response to the Disaster*; The Washington Post (Online): Washington, DC, USA, 2020.
19. Qiao, Z.; Fang, L.; Zhang, Y.; Yang, J.; Jiang, T.; Yuan, H. Spatio-temporal characteristics of forest fires in china between 2001 and 2017. *Ying Yong Sheng Tai Xue Bao J. Appl. Ecol.* **2020**, *31*, 55–64.
20. Palmer, W.C. *Meteorological Drought*; US Department of Commerce, Weather Bureau: Washington, DC, USA, 1965.
21. McKee, T.B.; Doesken, N.J.; Kleist, J. The relationship of drought frequency and duration to time scales. In Proceedings of the 8th Conference on Applied Climatology, American Meteorological Society, Boston, MA, USA, 17–22 January 1993.
22. Vicente-Serrano, S.M.; Beguería, S.; López-Moreno, J.I. A multiscalar drought index sensitive to global warming: The standardized precipitation evapotranspiration index. *J. Clim.* **2010**, *23*, 1696–1718. [[CrossRef](#)]
23. Yan, G.X.; Liu, Y.; Chen, X. Evaluating satellite-based precipitation products in monitoring drought events in Southwest China. *Int. J. Remote Sens.* **2018**, *39*, 3186–3214. [[CrossRef](#)]
24. He, B.; Lu, A.F.; Wu, J.J.; Zhao, L.; Liu, M. Drought hazard assessment and spatial characteristics analysis in China. *J. Geogr. Sci.* **2011**, *21*, 235–249. [[CrossRef](#)]
25. Belayneh, A.; Adamowski, J. Standard precipitation index drought forecasting using neural networks, wavelet neural networks, and support vector regression. *Appl. Comput. Intell. Soft Comput.* **2012**, *2012*. [[CrossRef](#)]
26. Bayissa, Y.; Tadesse, T.; Demisse, G.; Shiferaw, A. Evaluation of satellite-based rainfall estimates and application to monitor meteorological drought for the Upper Blue Nile Basin, Ethiopia. *Remote Sens.* **2017**, *9*, 669. [[CrossRef](#)]
27. Bai, X.; Shen, W.; Wu, X.; Wang, P. Applicability of long-term satellite-based precipitation products for drought indices considering global warming. *J. Environ. Manag.* **2020**, *255*, 109846. [[CrossRef](#)] [[PubMed](#)]
28. Sahoo, A.K.; Sheffield, J.; Pan, M.; Wood, E.F. Evaluation of the tropical rainfall measuring mission multi-satellite precipitation analysis (TMPA) for assessment of large-scale meteorological drought. *Remote Sens. Environ.* **2015**, *159*, 181–193. [[CrossRef](#)]
29. Dhakar, R.; Sehgal, V.K.; Pradhan, S. Study on inter-seasonal and intra-seasonal relationships of meteorological and agricultural drought indices in the rajasthan state of india. *J. Arid Environ.* **2013**, *97*, 108–119. [[CrossRef](#)]
30. Guo, H.; Bao, A.; Liu, T.; Chen, S.; Ndayisaba, F. Evaluation of PERSIANN-CDR for meteorological drought monitoring over china. *Remote Sens.* **2016**, *8*, 379. [[CrossRef](#)]
31. Rajabi, A. Analysis of SPI drought class transitions due to climate change. Case study: Kermanshah (iran). *Water Resour.* **2016**, *43*, 238–248. [[CrossRef](#)]
32. Zambrano, F.; Wardlow, B.; Tadesse, T.; Lillo-Saavedra, M.; Lagos, O. Evaluating satellite-derived long-term historical precipitation datasets for drought monitoring in chile. *Atmos. Res.* **2017**, *186*, 26–42. [[CrossRef](#)]
33. Tan, M.; Chua, V.; Tan, K.; Brindha, K. Evaluation of TMPA 3B43 and NCEP-CFSR precipitation products in drought monitoring over singapore. *Int. J. Remote Sens.* **2018**, *39*, 2089–2104. [[CrossRef](#)]
34. Begueria, S.; Vicente-Serrano, S.; Reig, F.; Latorre, B. Standardized precipitation evapotranspiration index (SPEI) revisited: Parameter fitting, evapotranspiration models, tools, datasets and drought monitoring. *Int. J. Climatol.* **2014**, *34*, 3001–3023. [[CrossRef](#)]
35. Vicente-Serrano, S.; McVicar, T.; Miralles, D.; Yang, Y.; Tomas-Burguera, M. Unraveling the influence of atmospheric evaporative demand on drought and its response to climate change. *WIREs Clim. Chang.* **2020**, *11*, e632. [[CrossRef](#)]
36. West, H.; Quinn, N.; Horswell, M. Remote sensing for drought monitoring & impact assessment: Progress, past challenges and future opportunities. *Remote Sens. Environ.* **2019**, *232*, 111291.
37. Jiang, S.; Ren, L.; Zhou, M.; Yong, B.; Zhang, Y.; Ma, M. Drought monitoring and reliability evaluation of the latest TMPA precipitation data in the Weihe River Basin, Northwest China. *J. Arid Land* **2017**, *9*, 256–269. [[CrossRef](#)]
38. Jiang, S.; Ren, L.; Xu, C.-Y.; Yong, B.; Yuan, F.; Liu, Y.; Yang, X.; Zeng, X. Statistical and hydrological evaluation of the latest Integrated Multi-satellite Retrievals for GPM (IMERG) over a midlatitude humid basin in South China. *Atmos. Res.* **2018**, *214*, 418–429. [[CrossRef](#)]
39. Wang, Z.; Zhong, R.; Lai, C.; Chen, J. Evaluation of the GPM IMERG satellite-based precipitation products and the hydrological utility. *Atmos. Res.* **2017**, *196*, 151–163. [[CrossRef](#)]



40. Duan, Z.; Tuo, Y.; Liu, J.; Gao, H.; Song, X.; Zhang, Z.; Yang, L.; Mekonnen, D. Hydrological evaluation of open-access precipitation and air temperature datasets using SWAT in a poorly gauged basin in Ethiopia. *J. Hydrol.* **2019**, *556*, 612–626. [\[CrossRef\]](#)
41. Ashouri, H.; Hsu, K.L.; Sorooshian, S.; Braithwaite, D.K.; Knapp, K.R.; Cecil, L.D.; Nelson, B.R.; Prat, O.P. PERSIANN-CDR daily precipitation climate data record from multisatellite observations for hydrological and climate studies. *Bull. Am. Meteorol. Soc.* **2015**, *96*, 69–83. [\[CrossRef\]](#)
42. Funk, C.; Peterson, P.; Landsfeld, M.; Pedreros, D.; Verdin, J.; Shukla, S.; Husak, G.; Rowland, J.; Harrison, L.; Hoell, A.; et al. The climate hazards infrared precipitation with stations—A new environmental record for monitoring extremes. *Sci. Data* **2015**, *2*, 1–21. [\[CrossRef\]](#) [\[PubMed\]](#)
43. Huffman, G.; Bolvin, D.; Nelkin, E.; Wolff, D.; Adler, R.; Gu, G.; Hong, Y.; Bowman, K.; Stocker, E. The TRMM multisatellite precipitation analysis (TMPA): Quasi-global, multiyear, combined-sensor precipitation estimates at fine scales. *J. Hydrometeorol.* **2007**, *8*, 38–55. [\[CrossRef\]](#)
44. Aadhar, S.; Mishra, V. High-resolution near real-time drought monitoring in South Asia. *Sci. Data* **2017**, *4*, 170145. [\[CrossRef\]](#)
45. Huffman, G.J.; Bolvin, D.T.; Braithwaite, D.; Hsu, K.; Joyce, R.; Xie, P.; Yoo, S.H. NASA global precipitation measurement (GPM) integrated multi-satellite retrievals for GPM (IMERG). *Algorithm Theor. Basis Doc.* **2015**, *4*, 26.
46. Hou, A.; Kakar, R.; Neeck, S.; Azarbarzin, A.; Kummerow, C.; Kojima, M.; Oki, R.; Nakamura, K.; Iguchi, T. The global precipitation measurement mission. *Bull. Am. Meteorol. Soc.* **2014**, *95*, 701–722. [\[CrossRef\]](#)
47. Peng, F.; Zhao, S.; Chen, C.; Cong, D.; Wang, Y.; Ouyang, H. Evaluation and comparison of the precipitation detection ability of multiple satellite products in a typical agriculture area of china. *Atmos. Res.* **2020**, *236*, 104814. [\[CrossRef\]](#)
48. Tang, G.; Clark, M.; Papalexiou, S.; Ma, Z.; Hong, Y. Have satellite precipitation products improved over last two decades? A comprehensive comparison of GPM IMERG with nine satellite and reanalysis datasets. *Remote Sens. Environ.* **2020**, *240*, 111697. [\[CrossRef\]](#)
49. Huffman, G.J.; Bolvin, D.T.; Braithwaite, D.; Hsu, K.; Joyce, R.; Kidd, C.; Nelkin, E.J.; Sorooshian, S.; Tan, J.; Xie, P. NASA Global Precipitation Measurement (GPM) Integrated Multi-satellite Retrievals for GPM (IMERG). In *Algorithm Theoretical Basis Document (ATBD) Version 06*; NASA/GSFC: Greenbelt, MD, USA, 2019.
50. Tan, J.; Huffman, G.; Bolvin, D.; Nelkin, E. Diurnal Cycle of IMERG V06 Precipitation. *Geophys. Res. Lett.* **2019**, *46*, 13584–13592. [\[CrossRef\]](#)
51. Chen, S.; Hong, Y.; Cao, Q.; Gourley, J.J.; Kirstetter, P.; Yong, B. Similarity and difference of the two successive v6 and v7 trmm multisatellite precipitation analysis performance over china. *J. Geophys. Res. Atmos.* **2013**, *118*, 13060–13074. [\[CrossRef\]](#)
52. Tan, J.; Petersen, W.A.; Tokay, A. A Novel Approach to Identify Sources of Errors in IMERG for GPM Ground Validation. *J. Hydrometeorol.* **2016**, *17*, 2477–2491. [\[CrossRef\]](#)
53. Lu, Y.; Jiang, S.; Ren, L.; Zhang, L.; Wang, M.; Liu, R.; Wei, L. Spatial and Temporal Variability in Precipitation Concentration over Mainland China, 1961–2017. *Water* **2019**, *11*, 881. [\[CrossRef\]](#)
54. Lu, J.; Jia, L.; Menenti, M.; Yan, Y.; Zheng, C.; Zhou, J. Performance of the standardized precipitation index based on the TMPA and CMORPH precipitation products for drought monitoring in china. *IEEE J. Sel. Top. Appl. Earth Obs. Remote Sens.* **2018**, *11*, 1387–1396. [\[CrossRef\]](#)
55. Wei, L.; Jiang, S.; Ren, L.; Yuan, F.; Zhang, L. Performance of Two Long-Term Satellite-Based and GPCC 8.0 Precipitation Products for Drought Monitoring over the Yellow River Basin in China. *Sustainability* **2019**, *11*, 4969. [\[CrossRef\]](#)
56. Schneider, U.; Schneider, U.; Becker, A.; Becker, A.; Finger, P.; Finger, P.; Rudolf, B. GPCC's new land surface precipitation climatology based on quality-controlled in situ data and its role in quantifying the global water cycle. *Theor. Appl. Climatol.* **2014**, *115*, 15–40. [\[CrossRef\]](#)
57. Chen, S.; Zhang, L.; Zhang, Y.; Guo, M.; Liu, X. Evaluation of tropical rainfall measuring mission (TRMM) satellite precipitation products for drought monitoring over the middle and lower reaches of the yangtze river basin, china. *J. Geogr. Sci.* **2020**, *30*, 53–67. [\[CrossRef\]](#)
58. Mosaffa, H.; Sadeghi, M.; Hayatbini, N.; Gorooh, V.; Asanjan, A.; Nguyen, P.; Sorooshian, S. Spatiotemporal variations of precipitation over iran using the high-resolution and nearly four decades satellite-based PERSIANN-CDR dataset. *Remote Sens.* **2020**, *12*, 1584. [\[CrossRef\]](#)

59. Yu, C.; Hu, D.; Liu, M.; Wang, S.; Di, Y. Spatio-temporal accuracy evaluation of three high-resolution satellite precipitation products in china area. *Atmos. Res.* **2020**, *241*, 104952. [[CrossRef](#)]
60. Yang, X.; Lu, Y.; Tan, M.; Li, X.; Wang, G.; He, R. Nine-year systematic evaluation of the GPM and TRMM precipitation products in the shuaishui river basin in east-central china. *Remote Sens.* **2020**, *12*, 1042. [[CrossRef](#)]
61. Jiang, S.; Wei, L.; Ren, L.; Xu, C.-Y.; Zhong, F.; Wang, M.; Zhang, L.; Yuan, F.; Liu, Y. Utility of integrated IMERG precipitation and GLEAM potential evapotranspiration products for drought monitoring over mainland China. *Atmos. Res.* **2020**, *247*, 105141. [[CrossRef](#)]



© 2020 by the authors. Licensee MDPI, Basel, Switzerland. This article is an open access article distributed under the terms and conditions of the Creative Commons Attribution (CC BY) license (<http://creativecommons.org/licenses/by/4.0/>).